nature communications

Article

https://doi.org/10.1038/s41467-025-59669-3

# Co-initiating-system dual-mechanism drives the design of printable entangled polymer multinetworks

Received: 21 December 2024

Accepted: 30 April 2025

Published online: 13 May 2025

Check for updates

An Wei[1,4], Qian Wang[1,4], Jupen Liu[2], Yuchan Huang[1], Haoxiang Li[1], Zhenhao Zhu[1], Tao Wang[3] & You Yu[1]

Entanglement significantly enhances the mechanical performance and functionality of both natural and synthetic materials. However, developing straightforward, versatile strategies for creating high-performance entangled polymer materials remains a challenge. Here, a co-initiating-system dual-mechanism strategy is designed for fabricating printable entangled polymer multinetworks. This thermal-light dual-initiation process benefits the synthesis of high-molecular-weight polymers and promotes the rapid formation of multinetworks within hydrogels. The resulting long polymer chains enable hydrogels with higher mechanical performance, lower stress relaxation, and activation energy compared to short polymer chain-contained samples. Such a method proves more effective than traditional self-thickening and strengthening techniques for enhancing hydrogel entanglements and is also compatible with additive manufacturing, enabling the design of complex 2D webs with adaptive mechanical performance and capable of detecting and sensing applications. This work provides an effective strategy for designing high-performance entangled polymer materials, which are set to impact numerous fields, from advanced sensing to material science and beyond.

Entanglement is a fundamental topological constraint in both natural and synthetic polymers. The formation of strong interactions among long polymer chains significantly enhances the stability of DNA helices, the structural integrity of protein folds[1–5], and the mechanical properties of polymeric rubbers, elastomers and plastics[6,7]. Importantly, these noncovalent interactions restrict chain movement under normal conditions but allow exceptional sliding and rearranging during mechanical deformations, greatly enhancing Young's modulus and energy dissipation-key characteristics for designing materials that are both strong and tough[8–11]. Inspired by these properties, many entangled polymer systems have been developed to create high-performance, robust materials for advanced applications[12,13]. For instance, engineered proteins are more likely to form entanglements within soft hydrogels, increasing stiffness and making them well-suited for bone and cartilage repair[14]. Likewise, highly entangled synthetic polymers with high viscosity are compatible with additive manufacturing[15], enabling spatially regulated properties such as adhesion[16,17], friction[18], and responsiveness-ideal for sensing and energy storage devices[19–21], and artificial scaffolds[22–25]. These pioneering advancements underscore the potential of high-entanglement polymer materials, opening avenues for applications in energy, engineering, electronics, and beyond[26–30].

Polymer entanglement, from a chemical perspective, primarily arises from the flexibility of polymer chains, multiple noncovalent interactions either among chains or with solvents, and the influence of specific chemical conditions[31–34]. Therefore, it is reasonable to predict that longer polymer chains, stronger interactions, and mild processing conditions are generally expected to promote higher degrees of entanglement in polymeric materials[35–37]. One straightforward method

[1]Key Laboratory of Synthetic and Natural Functional Molecule Chemistry of the Ministry of Education, College of Chemistry and Materials Science, Northwest University, Xi'an 710069, China. [2]College of Chemistry, Chongqing Normal University, Chongqing 401331, China. [3]School of Materials Science and Engineering, South China University of Technology, Guangzhou 510640, China. [4]These authors contributed equally: An Wei, Qian Wang. e-mail: yuyou@nwu.edu.cn

to achieve high entanglement in hydrogels is by directly incorporating high-molecular-weight polymers into hydrogel precursors, followed by initiating monomer polymerization[36,38,39]. This approach encourages entanglement between the introduced polymers and the newly formed chains. However, it heavily relies on the compatibility and specific interactions among all components, and the solubility of added polymers decreases as molecular weight increases. Furthermore, while this method generates noncovalent interactions, these polymers lack additional strong supramolecular or covalent bonds, limiting their mechanical performance and application potential. Introducing ring- and porous sphere-like structures, such as cyclodextrins, covalent organic frameworks, and microgels, presents another effective strategy to promote entanglement[40–43]. These structures encapsulate or penetrate small molecules, enabling polymerization within confined spaces and constraining two or more polymers within these frameworks without requiring specific interaction or solubility conditions. However, the large size, limited content, and nonuniform distribution of these components in precursors present challenges, as specific host-guest interactions and size-matching are often necessary for effective inclusion. More recently, in situ approaches using a single initiator at low concentrations or dual initiators at standard concentrations have shown promise in synthesizing high-molecular-weight, highly entangled polymers directly within hydrogels[35,44–47]. These methods avoid the need for additional components, with entanglement resulting solely from the in situ synthesis of high-molecular-weight polymers. However, these strategies typically use a single type of polymerization, limiting the flexibility to initiate multiple polymerizations with different components in one system, a feature crucial for forming hierarchical structures that further improve the mechanical performance of polymeric materials[48–51]. Additionally, the complex, multi-step preparation required by these methods is often unsuitable for designing intricate structures compatible with classic additive manufacturing techniques. Thus, developing straightforward, versatile strategies remains a critical challenge in creating high-performance polymer materials with extensive entanglement, exceptional mechanical properties, and enhanced printability.

In this work, we present a strategy termed the co-initiating-system dual-mechanism (CISDM) process for creating high-performance, printable entangled polymer multinetworks (PEPMNs). This approach utilizes the distinct initiation mechanisms of persulfate initiators in thermal and light-triggered polymerizations. At low temperatures, the slow polymerization of vinyl monomers forms short polymer radicals. Subsequent light irradiation then efficiently polymerizes the remaining monomers and enables the formation of multinetworks through phenol-coupling reactions. The resulting longer polymer chains significantly enhance mechanical strength, recovery, tear and creep resistance, anti-fatigue behavior, and low-stress relaxation. The proposed CISDM strategy proves more effective for improving hydrogel mechanics compared to conventional self-thickening and strengthening techniques. Additionally, PEPMNs exhibit lower activation energy than conventional samples, demonstrating sensitivity to chemical environments in terms of entanglement and mechanical performance. Moreover, the rapid, controllable photopolymerization in CISDM is compatible with additive manufacturing, enabling the fabrication of complex PEPMN structures. Leveraging these advantages, we successfully designed 2D hydrogel webs and 3D pyramid arrays capable of detecting and sensing different weight loads. To our knowledge, this is a report of a straightforward, broadly applicable CISDM strategy for developing highly entangled PEPMNs with high mechanical performance and enhanced printability.

## Results and discussion

Multiple initiation mechanisms, such as thermal and/or light initiation, within a single system enable the incorporation of diverse monomers and polymerizable components into a material by combining mechanistically distinct polymerization reactions[52,53]. These strategies have been widely employed for the one-pot synthesis of block copolymers and bulk materials[54]. At the same time, introducing hierarchical structures, such as contrasting multinetworks and entangled polymer networks, can significantly enhance the mechanical properties of polymer materials[12,32,55]. However, several issues should be considered in existing multiple-initiation systems for the preparation of high-performance polymer hydrogels. For instance, systems employ dual initiation mechanisms but are restricted to initiating only a single type of polymerization, such as radical or cationic polymerization, leading to the formation of just one network with moderate mechanical performance. Others rely on polymerization processes that are highly sensitive to environmental factors like oxygen and humidity, limiting their applicability in fabricating water-rich hydrogels in an open atmosphere. Although some systems allow sequential polymerization of distinct networks with different mechanisms, these processes are often slow. Additionally, sol-gel transitions typically occur during the first polymerization step, making them incompatible with additive manufacturing techniques used for printing complex structures. Furthermore, as mentioned above, incorporating entangled architectures in hierarchical tough hydrogels remains a challenge, despite their potential to enhance key mechanical properties such as strength, toughness, and Young's modulus. While multi-initiating systems provide versatility, they can also introduce complexity, making fabrication processes more intricate and less practical compared to single- or co-system approaches. Thus, there is a critical requirement to develop co-initiating-system multiple-mechanism strategies that enable the rapid formation of highly entangled and contrasting multinetworks, facilitating the design of printable, strong, and tough hydrogels.

### Co-initiating-system dual-mechanism process

Figure 1a and b illustrates a comparison of three strategies for producing PEPMNs: the traditional addition of high-molecular-weight polymer (AHMWP), the co-initiating-system single-mechanism (CISSM) process, and CISDM. Here, an aqueous solution of acrylamide monomer (AAm), gelatin, alginate, and a persulfate/ruthenium complex initiator serves as the model precursor to prepare these high-performance polymer multinetworks. In this system, AAm and gelatin create interpenetrating networks, while alginate further enhances the hydrogel's mechanical properties[16,56]. Despite using identical precursor components, these approaches yield different solubility and mechanical performance outcomes. In the CISDM strategy, the precursor is first held at a low temperature for a specified duration, and then exposed to visible light. Under low temperatures, persulfates decompose slowly, generating sulfate radicals (Supplementary Fig. 1) that initiate the gradual polymerization of vinyl monomers to form short polymer radicals. Subsequent light exposure triggers a rapid redox reaction between persulfates and ruthenium complexes[57,58]. The resulting sulfate radicals drive further polymerization of the remaining AAm monomers and extend the previously generated polymer radicals. Together, these dual mechanisms produce long, highly entangled PAAm chains, resulting in a transparent, highly viscous PAAm solution. Simultaneously, the oxidized ruthenium complexes initiate phenol-coupling in gelatin[59], establishing a robust, entangled multinetwork structure that enhances the mechanical properties of PEPMNs (Supplementary Fig. 2).

In contrast, CISSM employs a single initiation mechanism, yielding short PAAm chains under either thermal or light treatment. While this results in a transparent solution, the degree of entanglement and, consequently, mechanical strength, is limited. The direct addition of high-molecular-weight polymers also restricts solubility due to strong PAAm interactions, producing an opaque, white precursor with poor mechanical properties. Figure 1c contrasts the printability and load-bearing capacity of PEPMNs prepared using CISDM versus CISSM.

https://doi.org/10.1038/s41467-025-59669-3

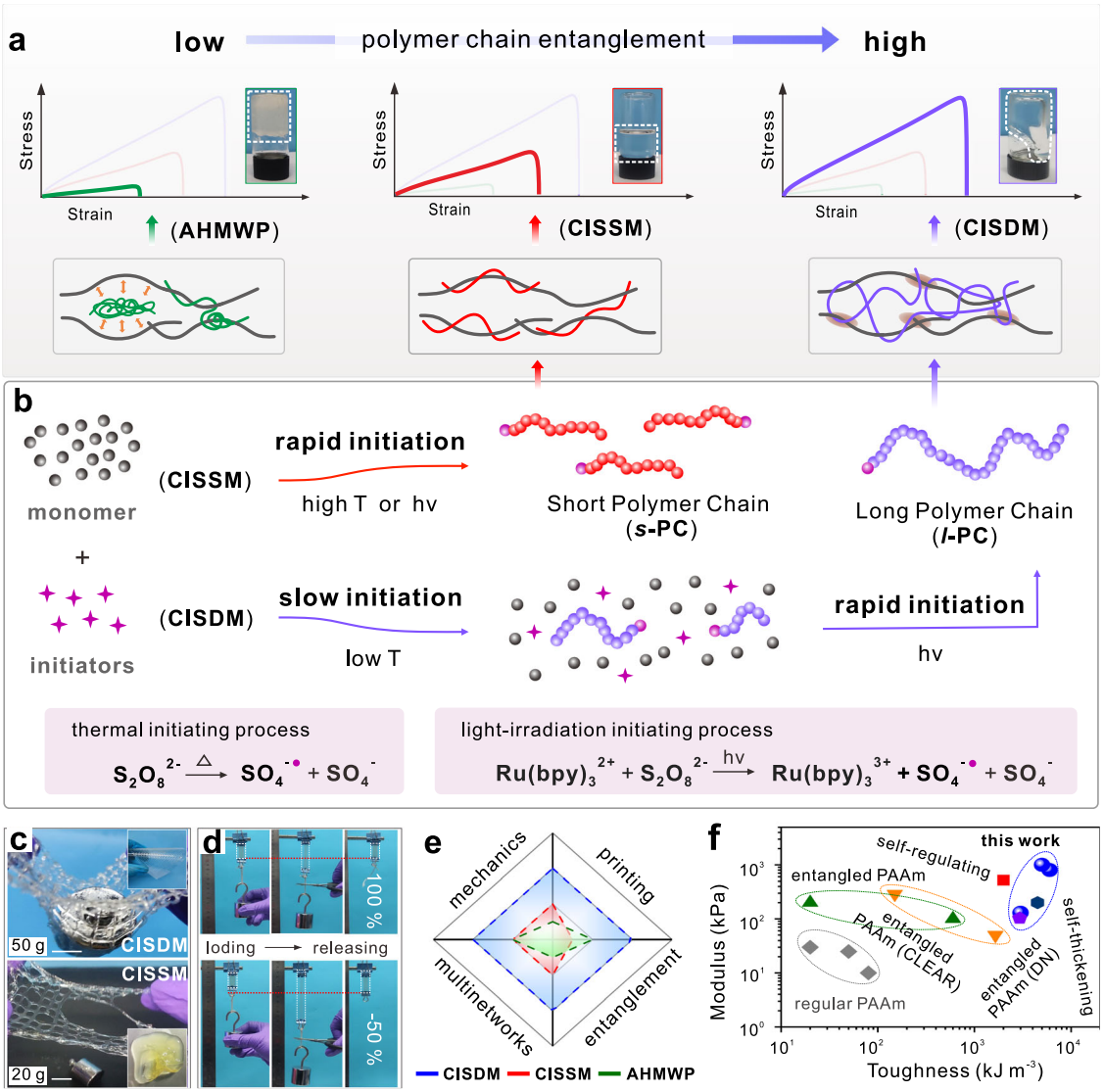


**Fig. 1 | Schematic illustration of printable entangled polymer multinetworks hydrogels via the co-initiating-system dual-mechanism process. a** Schematic diagram of polymer entanglement prepared by three strategies, respectively, and the mechanical comparison of PEPMNs. The stress-strain curves originate from the mechanical tests Fig. 4a in (Inset images are entangled polymers in water). **b** The specific polymerization processes of CISSM and CISDM strategies. **c** Digital images of 3D printed and load-bearing tests of PEPMNs prepared by CISDM and CISSM strategies, respectively. Scale bar = 1 cm. (The CISSM strategy incorporates a thickening agent into the precursor to enhance printability, while the inset image depicts a digital photograph of a sample printed without the addition of the thickening agent.) **d** Digital images of the recovery capability of PEPMNs prepared by CISSM and CISDM strategies, respectively. **e** Comparison of the mechanics, printable, entanglement, and multinetworks of PEPMNs prepared using the three strategies. **f** Comparison of their toughness and modulus with reported hydrogels.

While CISDM-prepared PEPMNs can support up to 50 g and maintain high-resolution printability, CISSM hydrogels can only support up to 20 g and exhibit reduced printability. Additionally, CISDM-prepared PEPMNs quickly recover their original shape after load release (Fig. 1d and Supplementary Movie 1). These findings underscore the advantages of CISDM over traditional and single-mechanism approaches for creating multinetwork polymers with high mechanical strength, printability, and entanglement (Fig. 1e). Compared with similar materials[35,36,39,45,46,48], PEPMNs demonstrate higher Young's modulus and toughness, highlighting the effectiveness of CISDM in achieving high entanglement and mechanical performance (Fig. 1f).

## Polymer chains versus entanglement

Rheology characterization in Fig. 2a reveals that the viscosity of the PAAm solution prepared using the CISDM strategy maintains a pronounced plateau across shear rates from 0.1 to 1 $s^{-1}$, followed by a sharp 200-fold decrease as the shear rate reaches 100 $s^{-1}$. In contrast, the viscosity of the CISSM-prepared sample shows a narrower plateau and gradually decreases over the full range of shear rates. This difference in viscosity profiles reflects the distinct entanglement/disentanglement behaviors under shear (Fig. 2b). In the CISDM strategy, the low concentration of initiator radicals promotes the formation of longer polymer chains (*l*-PC), resulting in greater entanglement and sustained viscosity across a broader shear range. By comparison, CISSM generates a higher concentration of radicals more rapidly, producing shorter polymer chains (*s*-PC) that disentangle more easily under shear forces. Figure 2c indicates that approximately 10% of AAm monomers convert to PAAm during low-temperature storage, with conversion reaching nearly 100% within 200 s upon subsequent light irradiation. This photopolymerization in CISDM mirrors that observed with single-light irradiation, suggesting that the low-temperature thermal initiation has no adverse effects. This dual-mechanism process is further validated by using phosphine oxides as a visible-light initiator: while they effectively initiate polymerization under light, they

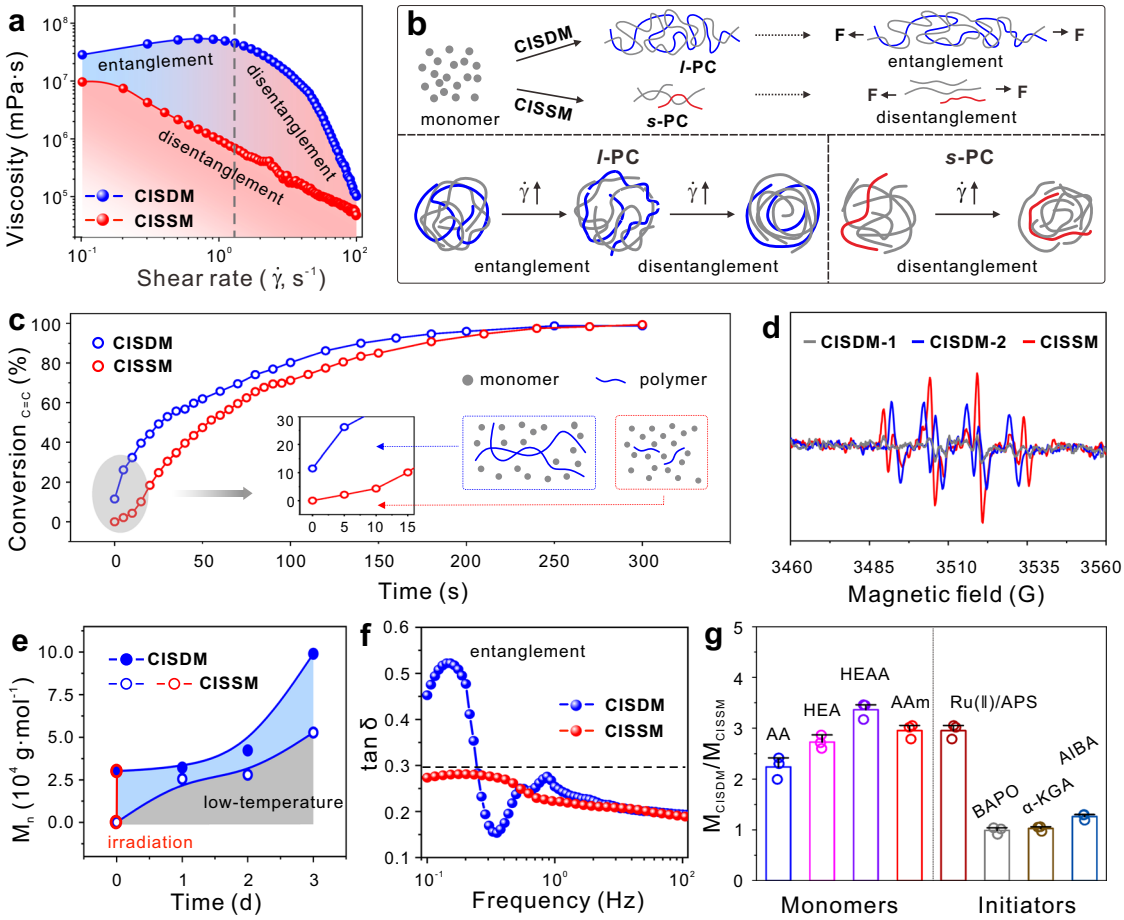


**Fig. 2 | Effect of polymer chain length on entanglement. a** Viscosity variation in different PAAm solutions with increasing shear rates ($\dot{\gamma}$). **b** Schematic diagram of the movement of long polymer chain (*l*-PC) and short polymer chain (*s*-PC) under different forces and shear rates. F presents the stretching force. **c** FT-IR conversion rates of C=C bonds in AAm monomers initiated by CISDM and CISSM strategies, respectively (Inset images are schematic illustrations of the specific components in these polymer precursors). **d** EPR spectra of sulfate radicals in different initiating processes. CISDM-1 indicates the low-temperature thermal initiating process, CISDM-2 and CISSM indicate the light-irradiation initiating process. **e** Number-average molecular weights ($M_n$) of *l*-PC-based and *s*-PC-based PAAm prepared by different initiation strategies and times. **f** Loss factor variation (tan $\delta$) of *l*-PC-based and *s*-PC-based PAAm under different frequencies. **g** Molecular weight variations of typical polymers and PAAm prepared by corresponding monomers and different initiators via the CISDM and CISSM strategies, respectively. Concentrations: [AAm] = 30 wt.%, [APS] = 88 mM and [Ru(II)]= 31.2 μM. ($n$ = 3 independent samples, and data are presented as mean ± SD in (**g**)).

cannot proceed at low temperatures alone (Supplementary Fig. 3). Therefore, no significant differences were observed in monomer conversion and mechanical performance when preparing hydrogels using the CISSM and CISDM strategies (Supplementary Figs. 4, 5).

The electron paramagnetic resonance spectra in Fig. 2d illustrate that the low-temperature thermal initiation in CISDM-1 generates a small number of sulfate radicals, resulting in a high molar ratio of AAm monomers to initiator radicals. This condition favors the synthesis of polymers with high molecular weight. In contrast, the subsequent photochemical initiation (CISDM-2) rapidly produces a high concentration of sulfate radicals, enabling fast and efficient polymerization of PAAm. Conversely, the CISSM strategy, which relies solely on high-temperature thermal initiation and light irradiation, leads to the rapid generation of highly concentrated sulfate radicals and fast polymerization within a short time. However, due to the low molar ratio of monomers to initiator radicals, this approach results in PAAm with lower molecular weight. The results of molecular weight characterization strongly support this conclusion. Figure 2e shows that the molecular weight of PAAm produced by CISSM is approximately 2.5 to $5 \times 10^4$ g mol$^{-1}$, while the CISDM approach increases the molecular weight to roughly $10 \times 10^4$ g mol$^{-1}$ with 3 d of storage, nearly double that achieved by CISSM (supplementary Table 1). Additionally, the highly entangled PAAm in CISDM solutions displays a high loss angle (tan δ) of up to 0.5 at low frequencies, whereas tan δ remains below 0.3 in CISSM samples[11,60–62], indicating greater energy is needed to disrupt the entangled structure in polymers (Fig. 2f). This enhanced entanglement through CISDM resembles that of CISSM systems with high monomer concentrations, where increased monomer content effectively boosts entanglement similarly to increasing polymer chain length (Supplementary Fig. 6). Moreover, it is found the CISDM strategy is broadly applicable for monomers, facilitating high entanglement across PAAm and other vinyl monomers using various typical initiators, but no significant difference in other single light or thermal initiators (Fig. 2g and Supplementary Fig. 7).

## Mechanical properties of PEPMNs hydrogels

Beyond its advantage in forming long polymer chains (*l*-PC), the CISDM strategy also supports the creation of multinetworks similar to those made via the visible-light-mediated CISSM approach (Supplementary Fig. 2). As mentioned in Supplementary Figs. 8–12, these multinetworks consist of PAAm (from AAm monomer radical polymerization) and gelatin (from tyrosine residue coupling reactions). These hydrogels, termed *s*-PEPMN and *l*-PEPMN, correspond to samples prepared via CISSM and CISDM strategies, containing *s*-PC and *l*-PC of PAAm, respectively. The *l*-PEPMN demonstrates a maximum stress of 400 kPa at a critical strain of 1200% under an optimized

https://doi.org/10.1038/s41467-025-59669-3

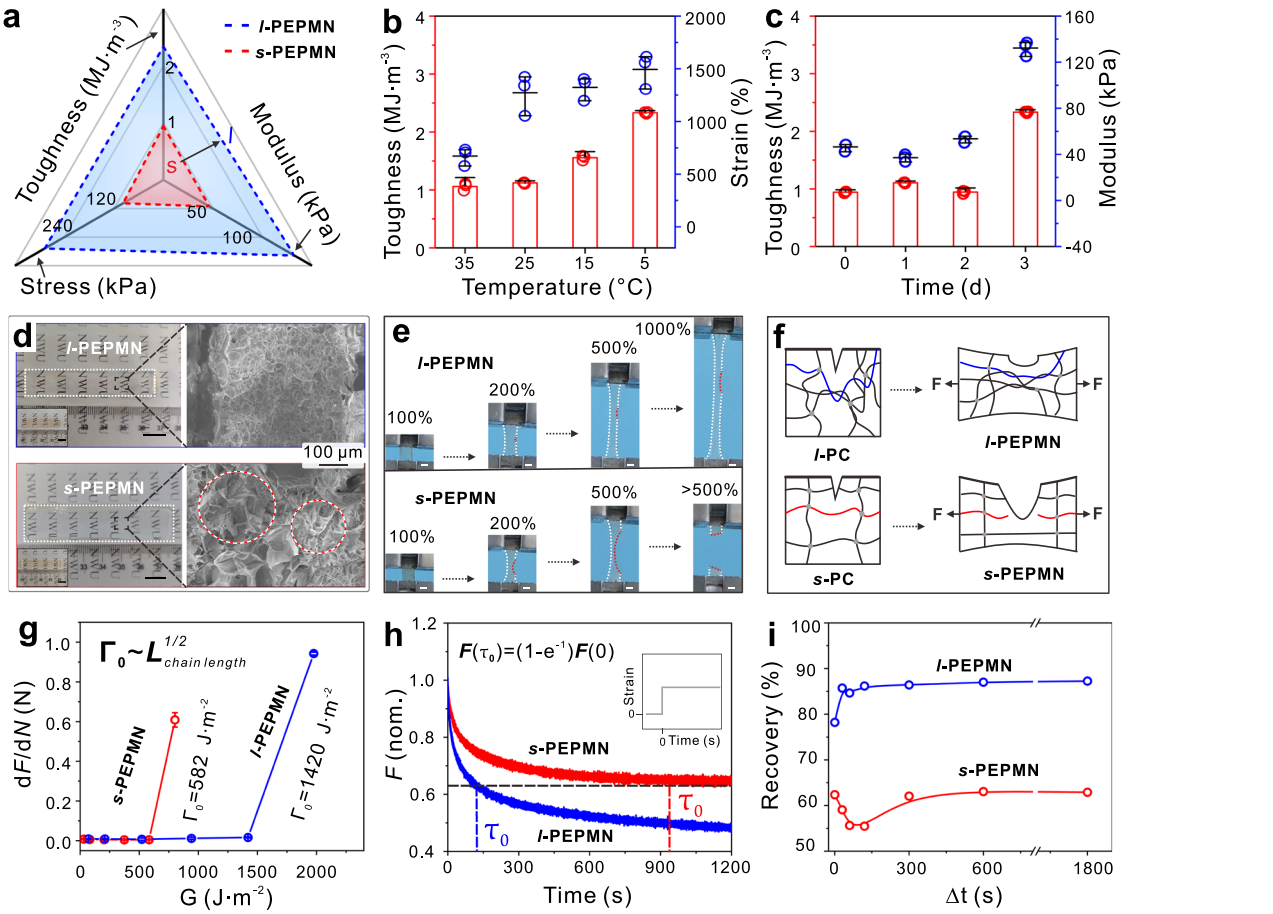


**Fig. 3 | Effects of entanglement on hydrogel mechanical performance. a** A comparison of the mechanical properties of *l*-PEPMN and *s*-PEPMN. Mechanical properties of PAAm hydrogels prepared at **b** different first thermal-initiation temperatures (35 °C for 2 h, 25 °C for 12 h, 15 °C for 24 h and 5 °C for 3 d) and **c** different times at 5 °C. Concentrations: [AAm] = 30 wt.%, [MBA] = 1 mM, [APS] = 88 mM and [Ru(II)]= 31.2 μM. **d** Swollen *l*-PEPMN and *s*-PEPMN hydrogels along with their SEM micrographs (Inset images are unswollen samples). **e** The snapshots of *l*-PEPMN and *s*-PEPMN under various deformations (Scale bar = 1 cm). Concentrations: [AAm] = 30 wt.%, [MBA] = 1 mM, [Gel] = 5 wt.%, [ALG] = 1 wt.%, [APS] = 88 mM and [Ru(II)]= 31.2 μM. **f** Schematic diagram of crack propagation of PEPMNs with different polymer chain lengths. **g** Fatigue thresholds ($\Gamma_0$) of PEPMNs with different chain lengths ($L_{chain\ length}$). G presents the toughness threshold. **h** Normalized stress relaxation (*F*) PEPMNs with different chain lengths (Inset image shows that constant strain applied) $\tau_0$ present the stress relaxation times. **i** Recovery rate of intermittent cycles of PEPMNs with different chain lengths. ($n = 3$ independent samples, and data are presented as mean ± SD in (**b**), (**c**) and (**g**)).

preparation condition (Supplementary Fig. 12). The mechanical comparison in Fig. 3a highlights that significant differences in properties arise between the hydrogels due to the presence of *s*-PC and *l*-PC, despite both PEPMNs being constructed with similar double-network structures. Figure 3b and c show that the toughness, maximum strain, and Young's modulus of *l*-PEPMN increase nearly threefold compared to *s*-PEPMN when the initial thermal initiation temperature is reduced from 35 °C to 5 °C, coupled with extended storage times of up to 3 days. These conditions favor *l*-PC formation, enhancing the network's mechanical resilience (Supplementary Figs. 13, 14). Moreover, the *l*-PEPMN hydrogel exhibited a lower swelling ratio due to chain entanglement acting as partial physical cross-linking points (Supplementary Fig. 15), while simultaneously demonstrating a homogeneous network architecture, as confirmed by scanning electron microscopy (SEM) characterization. In contrast, *s*-PEPMN hydrogels displayed a heterogeneous porous structure, with distinctly observable macroporous and microporous domains under SEM analysis (Fig. 3d). This comparison visually supports the role of high polymer chain entanglement in enhancing the mechanical performance of PEPMN hydrogels.

In tear-resistance testing, *l*-PEPMN shows no noticeable crack propagation even when stretched to over 1000% strain, whereas *s*-PEPMN displays significant crack propagation and fails around 500% strain (Fig. 3e). This performance enhancement in *l*-PEPMN is attributed to the high entanglement of *l*-PC, which efficiently dissipates mechanical energy during large deformation (Fig. 3f). Conversely, *s*-PC contributes less to network entanglement, resulting in obvious crack propagation and a structure that breaks more easily under small strains. Anti-fatigue testing further supports this difference: The fatigue threshold ($\Gamma_0$), which correlates with polymer chain length ($L_{chain\ length}$), is 1420 J m$^{-2}$ for *l*-PEPMN, approximately 2.5 times higher than that of *s*-PEPMN (Fig. 3g, Supplementary Fig. 16 and Note 1). The *l*-PC gives *l*-PEPMN a relaxation time ($\tau_0$) of 125 s, significantly lower than the 925 s observed for *s*-PEPMN, reflecting high energy dissipation (Fig. 3h). *l*-PEPMN exhibits improved resistance to creep, maintaining smaller strain levels under constant stress compared with that of *s*-PEPMN (Supplementary Fig. 17). Furthermore, *l*-PEPMN has lower hysteresis and recovers 85% of its original shape within 20 s when stretched, whereas *s*-PEPMN requires 300 s (Fig. 3i and Supplementary Fig. 18). The mechanical properties of PEPMN hydrogels remain stable throughout the cyclic swelling-drying treatment (Supplementary Fig. 19). These achieved results indicate a significant difference in the mechanical properties of *l*-PC- and *s*-PC-containing PEPMNs, despite both featuring interpenetrated polymer multinetworks (as shown in Fig. 3f). This difference can be attributed to the varying degrees of entanglement in these PEPMNs. The *l*-PC component induces a higher degree of entanglement, contributing more effectively to mechanical energy dissipation through the synergistic effect of polymer

https://doi.org/10.1038/s41467-025-59669-3

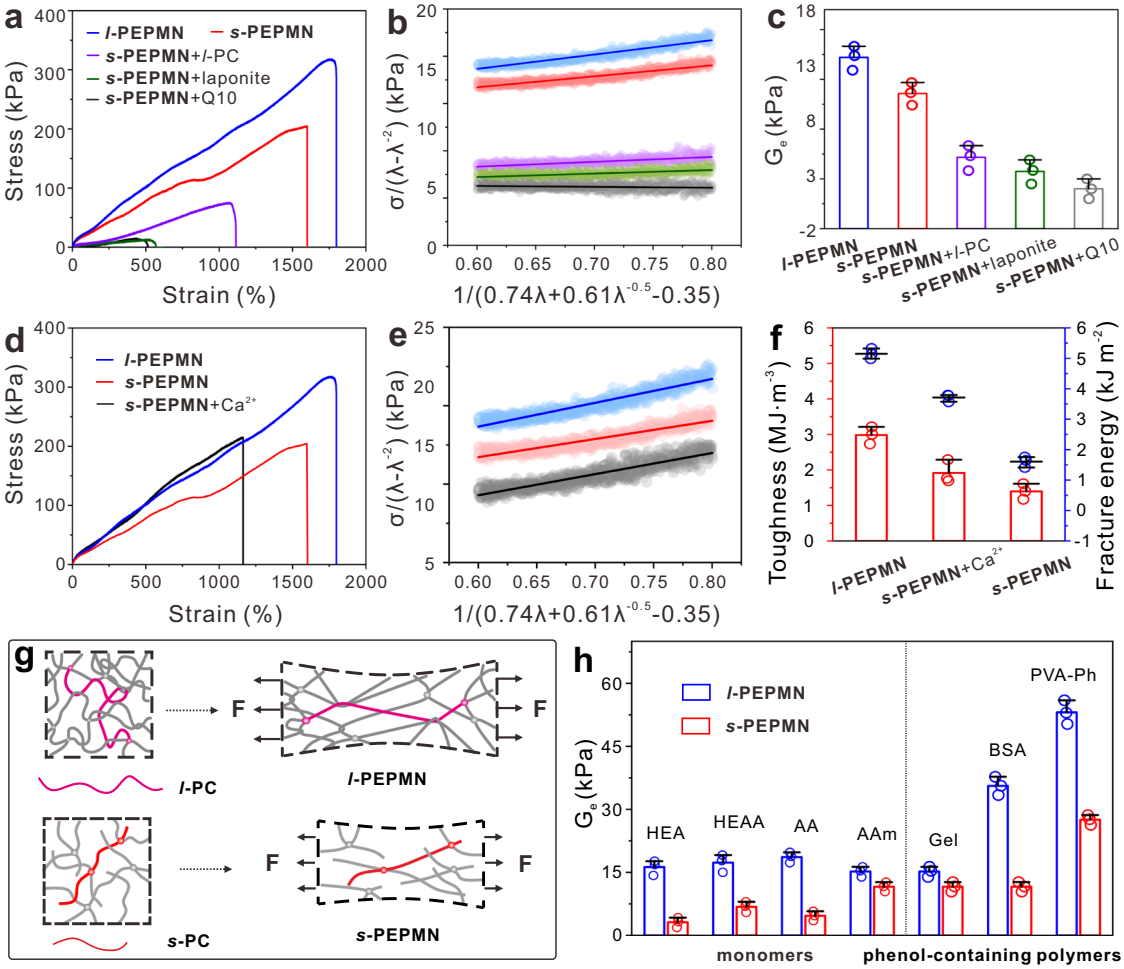


**Fig. 4 | Mechanical characterization of interactions between polymer chains.** **a** Stress-strain curves of hydrogels prepared by different thickening systems. **b** The variations of $\sigma/(\lambda-\lambda^{-2})$ as a function as $1/(0.74\lambda + 0.61\lambda^{-0.5}-0.35)$ and the corresponding linear fitting curve with different thickening systems. (where $\sigma$ represents the engineering stress of hydrogel, λ is the stretchability, $G_x$ and $G_e$ refer to the shear modulus contributed from crosslinks and entanglements, respectively.) **c** The $G_e$ of hydrogel with different thickening systems. **d** Stress-strain curves of hydrogel with different physical interaction systems. **e** The variations of $\sigma/(\lambda-\lambda^{-2})$ as a function as $1/(0.74\lambda + 0.61\lambda^{-0.5}-0.35)$ and the corresponding linear fitting curve with different physical interaction systems. **f** Comparison of toughness and fracture energy of hydrogels with different physical interaction systems. Apply 100 μL of 1 mol $L^{-1}$ $CaCl_2$ to the front and back surfaces of the *s*-PEPMN. **g** Schematic illustration of the variations in hydrogel network structures during stretching. **h** The $G_e$ of hydrogel with different vinyl monomers and phenol-containing polymers. ($n = 3$ independent samples, and data are presented as mean ± SD in (**b**), (**c**), (**e**), (**f**), and (**h**)).

chains disentanglement and rigid networks disruption. In contrast, similar to typical reported.

## Mechanical characterization of entanglement

Multinetwork hydrogels, *s*-PC results in a lower degree of entanglement, where mechanical energy dissipation primarily relies on the disruption of rigid networks[32,48,63]. Consequently, *s*-PC-containing PEPMNs exhibit moderate mechanical performance compared to those prepared using the CISDM strategy.

Then, the study of entanglement-dynamic viscoelastic behavior quantitatively illustrates how entanglement impacts PEPMN performance. Figure 4a demonstrates that the high entanglement in *l*-PEPMN enables it to exhibit high mechanical performance compared to *s*-PEPMN and its composites with conventional thickening and strengthening agents. These additives, rather than enhancing strength, impede the formation of strong hydrogels due to their lack of efficient interactions with PEPMNs (Supplementary Fig. 20). Consequently, the maximum stress and strain of these composites are only one-seventh and one-fourth, respectively, of those observed in *l*-PEPMN samples. Stress-strain analysis using the Rubinstein-Panyukov model (Fig. 4b, c and Supplementary Note 2) demonstrates that *l*-PEPMN achieves significantly higher entanglement factors than other samples, with the $G_e$ factor reaching about 15 kPa approximately four times that of *s*-PEPMN with *l*-PC and laponite. This high $G_e$ factor reflects increased shear modulus from entanglement. Additionally, the incorporation of polyquaternium 10 (Q10) severely compromises mechanical performance, with the $G_e$ factor decreasing from 12 kPa to less than 0 kPa as Q10 concentration rises, indicating weakened entanglement strength. As shown in Fig. 4d, while the alginate component forms strong ionic coordination with $Ca^{2+}$, it does not lead to significant entanglement improvement in comparison with *s*-PEPMN and *l*-PEPMN samples. The $G_e$ factors follow the order of *l*-PEPMN > *s*-PEPMN > *s*-PEPMN + $Ca^{2+}$, indicating minimal entanglement contribution from the alginate chain themselves and alginate-$Ca^{2+}$ network (Fig. 4e). However, the interaction between alginate and $Ca^{2+}$ does enhance mechanical fracture energy by four times, maintaining a toughness comparable to that of *s*-PEPMN due to the formation of additional alginate-$Ca^{2+}$ network (Fig. 4f). Moreover, the CISDM strategy can also be combined with high-concentration monomers to in-situ regulate mechanical properties (Supplementary Fig. 21). Overall, these findings highlight the pivotal role of *l*-PC in enhancing entanglement within PEPMNs, which significantly improves energy dissipation during large deformations

https://doi.org/10.1038/s41467-025-59669-3

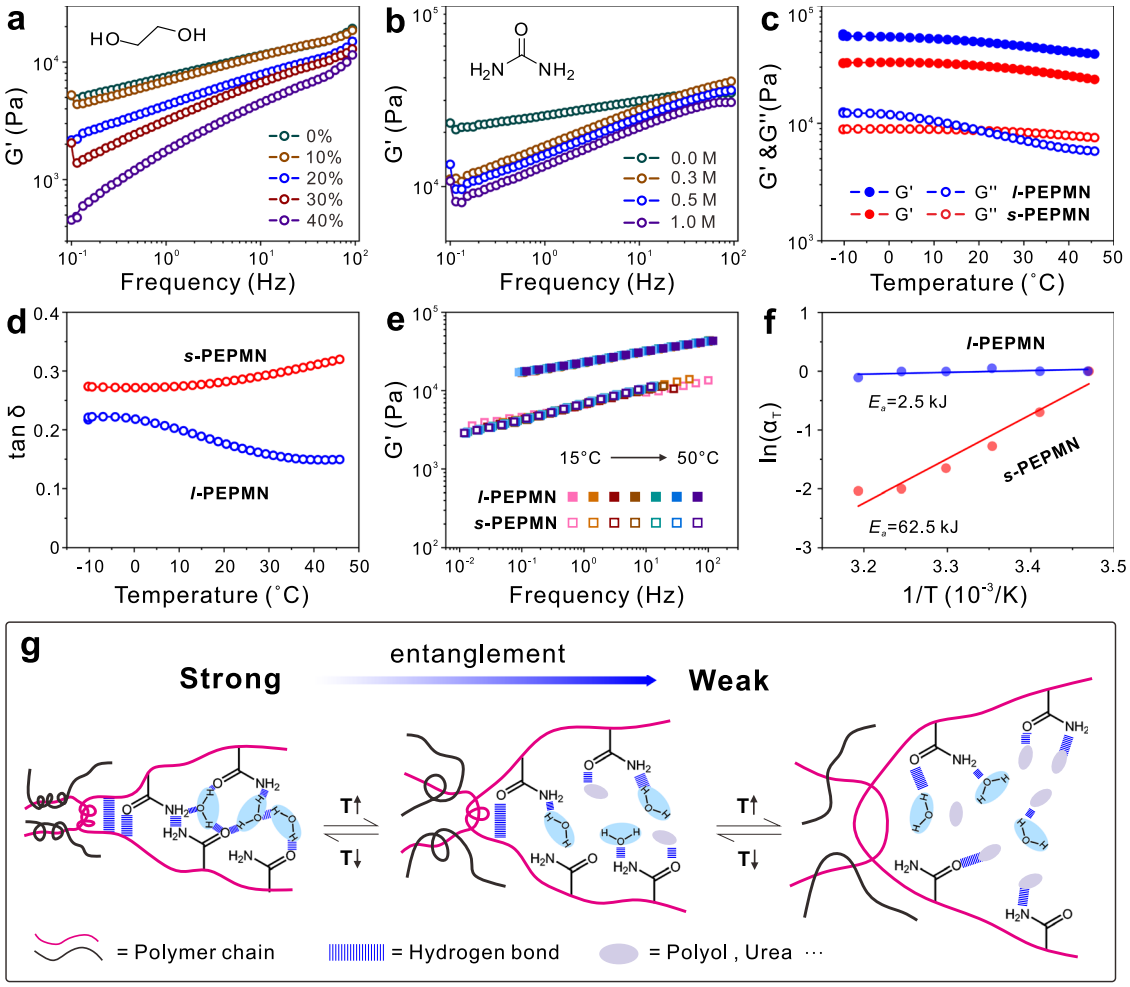


**Fig. 5 | Effects of chemical environments on entanglement.** Rheological characterization of PEPMNs prepared with different concentrations of **a** ethylene glycol and **b** urea solutions at different frequencies, respectively. **c** Storage (G') and loss (G'') moduli, and **d** loss factor (tan $\delta$) of PEPMNs with different chain lengths at different temperatures. **e** Storage modulus (G') at different frequencies for PEPMNs with varying chain lengths, determined using TTS shifts at a reference temperature of 15 °C. **f** Plot of ln $\alpha_T$ vs. 1/T on a log-log scale. $\alpha_T$, T, and $E_a$ present the shift factor, thermodynamic temperature scale and activity energy, respectively. The solid line represents the linear fitting line. **g** Schematic representation of the effect of chemical environment on polymer chain entanglement. Concentrations: [AAm] = 30 wt.%, [MBA] = 1 mM, [APS] = 88 mM and [Ru(II)]= 31.2 μM.

(Fig. 4g). The adhesive properties further support this, with *l*-PC providing additional adhesion sites and effectively dissipating mechanical energy at interfaces (Supplementary Fig. 22)[64,65]. More importantly, Fig. 4h, Supplementary Figs. 23 and 24 exhibit a similar trend in the enhancement of polymer chain entanglement in PEPMNs prepared with various typical vinyl monomers (i.e., HEAA, HEA and AAm) and phenol-containing polymers (i.e., Gel, BSA and PVA-Ph). All PEPMNs fabricated using the CISDM strategy exhibit a higher degree of entanglement and high mechanical strength compared to those prepared using the CISSM strategy. This finding suggests that the CISDM strategy promotes the formation of *l*-PC, significantly enhancing $G_e$ values and entanglement degrees, establishing it as a versatile and effective approach for designing high-performance polymer materials.

## Entanglement versus Chemical Environment

Furthermore, the effects of chemical environments on entanglement and mechanical properties were systematically evaluated through rheological characterization. As shown in Figs. 5a and 5b, demonstrate that the storage modulus (G′) of *l*-PEPMN gradually decreases as ethylene glycol and urea concentrations increase to 40% and 1.0 M, respectively. This reduction is attributed to the strong interactions between these additives and water, which disrupt noncovalent interactions between polymers and water, leading to a decrease in *l*-PC entanglement in PEPMNs (Supplementary Figs. 25 and 26). Quantitative force analysis using single-molecule force spectroscopy further supports this variation[66]. PAAm exhibits strong interactions with water and distinct solvation behaviors in polar (water) versus nonpolar solvents compared to alginate and gelatin components. This suggests that ethylene glycol and urea significantly interfere with PAAm-water interactions, weakening polymer entanglement upon their introduction (Supplementary Fig. 27). Consequently, the reduction in PAAm entanglement within PEPMNs leads to a decline in hydrogel mechanical strength (Supplementary Fig. 28). This trend is consistent with the modulus reductions observed at higher temperatures, where disrupted noncovalent interactions decrease entanglement (Fig. 5c). Additionally, the high degree of entanglement in *l*-PEPMN results in a marked decrease in the loss modulus (G″) with rising temperature, as reflected in tan δ values, which decrease progressively during heating (Fig. 5d). In contrast, the lower entanglement in *s*-PEPMN shows minimal temperature sensitivity, with tan δ remaining constant or even increasing with heating. Lower temperatures are associated with extended durations of action, corresponding to lower frequencies. Similar findings have been noted on the rheological frequency curve (Supplementary Fig. 29). Time-temperature rheological characterization in Figs. 5e and 5f reveals that chemical crosslinking in the samples enhances their mechanical stability, resulting in minimal variation in G′

https://doi.org/10.1038/s41467-025-59669-3

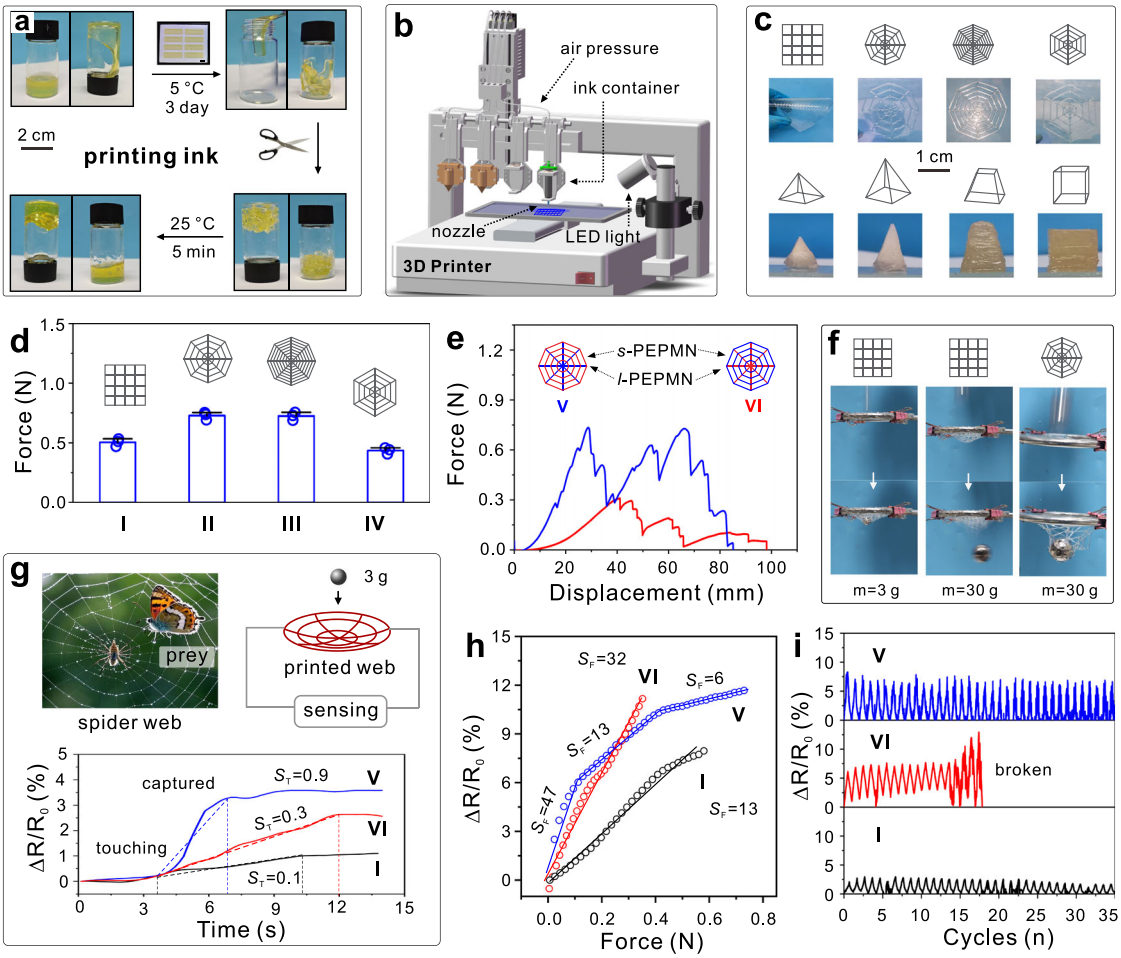


**Fig. 6 | Structured design of PEPMNs-based flexible sensing devices. a** Schematic illustration of 3D printing ink. **b** The illustration of the 3D printer for preparing structured PEPMNs hydrogels. **c** Representative 2D patterns and 3D architectures fabricated via 3D printing (Scale bar = 1 cm). **d** Maximum load-bearing capacity measurements of printed grid and spiderweb structures. **e** Material-specific design strategy demonstrating the use of *l*- and *s*- PEPMN compositions to fabricate spiral and radial hydrogel threads. **f** Free-fall impact test of steel balls on PEPMNs-printed grid and spiderweb structures. m presents the mass of balls. **g** Bioinspired sensor design concept mimicking the morphology of spiderwebs for sensing applications ($S_T = (\Delta(\Delta R/R_0)/\Delta T)$). **h** Sensitivity characterization and operational range assessment of PEPMNs-based sensors ($S_F = (\Delta(\Delta R/R_0)/\Delta F)$). **i** Cyclic stability evaluation demonstrating the long-term durability of the sensor system. $R_0$, $\Delta R$, $\Delta T$ and $\Delta F$ represent the original resistance, and the changes in resistance, time, and force, respectively. ($n = 3$ independent samples, and data are presented as mean ± SD in (**d**)).

across different frequencies. Moreover, although both PEPMNs exhibit overlapping G′-frequency curves, forming single master curves, *l*-PEPMN's high entanglement yields an activation energy ($E_a$) of just 2.5 kJ only one-thirtieth of that for *s*-PEPMN. The incorporation of alginate into the system resulted in the reinforcement of the fixed entanglement formed by covalent and hydrogen bonding interactions among polyacrylamide (PAAm) chains (Supplementary Fig. 30). This observation serves to substantiate the significant connection between entanglement and intermolecular bonding interactions. These findings suggest that, beyond polymer chain length (Supplementary Fig. 31), the chemical environment, which strongly influences noncovalent polymer-solution interactions, significantly impacts the entanglement behavior of polymer materials (Fig. 5g).

## Applications of PEPMNs in sensing devices

Also, the CISDM strategy with *l*-PC reduces the gelation time to approximately 7 s, faster than 12 s required by the light-mediated CISSM (Supplementary Fig. 32). This improvement facilitates the printing of complex structures using 3D extrusion techniques combined with a visible-light initiation process. As shown in Fig. 6a and Supplementary Fig. 33, the liquid precursor ink initially has low viscosity and solidifies at 5 °C over three days. However, the slow initiation process during this low-temperature thermal polymerization results in a low degree of polymerization and crosslinking. This allows the solidified ink to transition back to a highly viscous state after being cut and warmed to room temperature for several minutes (Supplementary Fig. 34). Once extruded through a nozzle, visible light immediately triggers multinetwork formation, enabling the precise fabrication of PEPMNs with >95% accuracy in a layer-by-layer manner (Fig. 6b, Supplementary Figs. 35, 36, and Table 2). Leveraging high entanglement, multinetwork structure, and excellent printability, this approach successfully fabricates PEPMNs with hierarchical 2D grids, webs, and 3D architectures (Fig. 6c). The mechanical strengths of these PEPMN structures can be fine-tuned by adjusting the predesigned models, achieving maximum force tolerances between 0.4 and 0.8 N (Fig. 6d, Supplementary Figs. 37, 38). A mechanical comparison of different 2D web designs reveals that maximum force tolerance depends primarily on radial rather than spiral lines (Fig. 6e and Supplementary Fig. 39). Notably, the force tolerance of the converse PEPMN, which used the mechanically weaker *s*-PC for radial lines, was only one-third that of webs with *l*-PC radial lines. Ball-drop experiments visually support these findings (Fig. 6f, Supplementary Fig. 40 and Supplementary Movie 2). The *l*-PC-based PEPMN grid successfully supported a 3 g ball, while its web structure withstood a 30 g load. In contrast, the *s*-PC-

based webs failed to support even the 3 g ball. Moreover, inspired by the prey-detecting function of spider webs, PEPMNs are also explored for object catching and sensing (Supplementary Figs. 41, 42). Their sensing performance could be modulated from 0.1 to 0.9 by tailoring specific structures and materials (Fig. 6g). Notably, the *l*-PC-based PEPMN webs demonstrated higher sensitivity under low forces and a broader detection range compared to control samples. Additionally, they exhibited greater stability during cyclic testing, making them a more reliable choice for robust sensing applications (Figs. 6h, i).

In conclusion, we have developed a versatile and straightforward CISDM strategy using a dual thermal-light initiation system with persulfate initiators to create high-performance PEPMNs. This approach facilitates the in-situ generation of *l*-PC substantially increasing entanglement within the hydrogels. The resulting multi-network polymers demonstrate high strength, toughness, printability, and low hysteresis, making them ideal for building hierarchical structures and high-performance sensors. The CISDM strategy offers several distinct advantages over existing methods for creating entangled polymers. First, it uses a co-initiating-system with dual initiation mechanisms, suggesting that other initiators with multiple initiation capabilities could also be leveraged to design strong, tough polymer materials by promoting entanglement. Secondly, CISDM combines conventional radical polymerization with a phenol-coupling reaction, allowing a wide variety of vinyl monomers and phenol-containing materials to be incorporated for designing highly entangled, mechanically robust materials. Lastly, the rapid and controllable photochemistry in CISDM is highly compatible with standard extrusion printing techniques, making it feasible to construct complex device architectures using common additive manufacturing methods, such as stereolithography and laminated object manufacturing. We believe this CISDM strategy and the resulting PEPMNs will significantly advance the development of strong, resilient materials, paving the way for innovative applications in fields such as sensing, medicine, electronics, and energy.

## Methods

### Materials

Gelatin (type A, ~300 g Bloom from porcine skin, Sigma-Aldrich), bovine serum albumin (BSA), sodium alginate (180947, G/M = 1.02, Sigma-Aldrich), N, N′-Methylenebisacrylamide (MBA), acrylamide (AAm), acrylic acid (AA), 2-hydroxyethyl acrylate (HEA), N-(2-Hydroxyethyl) (HEAA), tris(bipyridine)ruthenium(II) chloride ($Ru(bpy)_3Cl_2$), Phenylbis(2,4,6-trimethylbenzoyl)phosphine Oxide (BAPO), 2-ketoglutaric acid (α-KGA), 2,2′-azobis(2-methylpropionamidine) dihydrochloride (AIBA), and ammonium persulfate (APS), all sourced from Admas. Polyvinyl alcohol (~145,000 g $mol^{-1}$) and other chemicals were obtained from Sinopharm Chemical Reagent Co. Ltd. All purchased materials are analytical reagent grade and used without further purification.

### Preparation of phenol-containing polyvinyl alcohol

typical synthesis process of PVA-1% Ph (i.e., PVA with 1% phenol in molecular structure) is as follows: 10 g (0.7 mmoL) of PVA powder was first mixed with 100 mL of N-methylpyrrolidone at 100 °C by vigorous mechanical stirring. When PVA was fully dissolved, the temperature was decreased to 70 °C. 4-Dimethy-laminopyridine (0.28 g, 2.3 mmoL) and succinic anhydride (0.24 g, 2.4 mmoL) were then added to the above mixture for 24 h stirring. After being cooled down to room temperature, the achieved mixture was added dropwise to ethyl acetate (~500 mL). The precipitate was collected and dried at 70 °C for 2 h in an oven. The obtained product was fully redissolved in 100 mL of DI water at 70 °C by mechanical stirring for 2 h. When decreasing the temperature to 30 °C, N-hydroxysuccinimide (0.56 g, 4.8 mmoL), tyramine (0.66 g, 4.8 mmoL), and 1-ethyl-3-(3-dimethylaminopropyl) carbodiimide (0.92 g, 4.8 mmoL) were added to the above solution. After further 24 h stirring, the resultant mixture was introduced dropwise to ethanol (~500 mL). The generated precipitate was collected and washed by ethanol twice. The final PVA-1% Ph was obtained by completely drying the collected precipitate at 70 °C in an oven.

### Preparation of PEPMNs Using the CISDM and CISSM Strategies

0.5 g of gelatin and 0.1 g of alginate were vigorously stirred in 10 mL of hot water at 60 °C to form a transparent solution. After cooling to room temperature, 3 g of AAm, 1.54 mg of MBA, 0.2 mg of Ru(II), and 0.2 g of APS were added sequentially with stirring to completely dissolve to form a clarified, transparent solution. Next, the solution was centrifuged for 2 min at 18,800 × g to remove air bubbles and injected into a polytetrafluoroethylene mold (8 mm × 40 mm × 2 mm). Finally, the mixture was stored at 5 °C for a predetermined time and cured under visible light (452 nm wavelength, 15 mW $cm^{-2}$) for a predetermined time to obtain *l*-PEPMN. Without low-temperature pretreatment, the mixture is cured under visible light (452 nm wavelength, 15 mW $cm^{-2}$) for a predetermined time to obtain *s*-PEPMN. Other PEPMNs from typical vinyl monomers and phenol-containing polymers were also prepared using the method described above.

### Preparation of PEPMN hydrogels by traditional high-molecular-weight polymer addition (AHMWP)

To achieve the PEPMN hydrogel preparation, *l*-PC PAAm was first synthesized using a process similar to the CISDM strategy but without the addition of a crosslinking agent. As a high-molecular-weight additive, 0.2 g of *l*-PC, 0.5 g of gelatin, and 0.1 g of alginate were vigorously stirred in 10 mL of hot water at 60 °C. After cooling to room temperature, 3 g of AAm, 1.54 mg of MBA, 0.2 mg of Ru(II), and 0.2 g of APS were sequentially added with stirring until fully dissolved, forming a clear, transparent solution. The solution was then centrifuged at 18,800 × g for 2 min to remove air bubbles before being injected into a polytetrafluoroethylene mold (8 mm × 40 mm × 2 mm). Finally, the mixture was cured under visible light (452 nm wavelength, 15 mW $cm^{-2}$) for a predetermined time to obtain the hydrogel samples.

### Preparation of PEPMN Hydrogels Using BAPO as the Single Photosensitive Initiator

0.5 g of gelatin and 0.1 g of alginate were vigorously stirred in 10 mL hot water at 60 °C to form a transparent solution. After cooling to room temperature, 3 g of AAm, 1.54 mg of MBA, and 0.3 g of BAPO were added sequentially with stirring to completely dissolve to form a clarified, transparent solution. Next, the solution was centrifuged for 2 min at 18,800 × *g* to remove air bubbles and injected into a polytetrafluoroethylene mold (8 mm × 40 mm × 2 mm). Finally, the mixture was stored at 5 °C for a predetermined time and cured under visible light (452 nm wavelength, 15 mW $cm^{-2}$) for a predetermined time to obtain BAPO-1 (CISDM). Without low-temperature pretreatment, the mixture is cured under visible light (452 nm wavelength, 15 mW $cm^{-2}$) for a predetermined time to obtain BAPO-2 (CISSM).

### Preparation of thickening-contained PEPMN hydrogels

0.5 g of gelatin, 0.1 g of alginate, and 0.2 g of thickening agent (Q10 or laponite) were vigorously stirred in 10 mL of hot water at 60 °C to form a transparent solution. After cooling to room temperature, 3 g of AAm, 1.54 mg of MBA, 0.2 mg of Ru(II), and 0.2 g of APS were added sequentially with stirring to completely dissolve to form a clarified, transparent solution. Next, the solution was centrifuged for 2 min at 18,800 × *g* to remove air bubbles and injected into a polytetrafluoroethylene mold (8 mm × 40 mm × 2 mm). Finally, the mixture is cured under visible light (452 nm wavelength, 15 mW $cm^{-2}$) for a predetermined time to obtain a thickened controlled experimental hydrogel.

### 3D Printing of PEPMNs

The 3D printing of PEPMNs was performed using a lab-made direct-ink-write 3D printer (Fig. 6b). All 3D structures were designed by CINEMA 4D software. Precursor materials, *l*-PEPMN (stored for 3 days at 5 °C) and *s*-PEPMN (thickened with 4 wt.% ALG), were loaded into 10 ml syringes with 210 μm nozzles after degassing at 18,800 × *g*. The syringe was connected to a pressure supply and mounted on the robot's head. User-defined PEPMNs-based structures were printed by controlling pressure (3 kPa), robot movement (20 mm $s^{-1}$), and light (452 nm) irradiation.

### Characterizations

The in-situ FT-IR spectra were obtained using a Bruker INVENIOR spectrometer to monitor the real-time polymerization of AAm under visible light (452 nm, 15 mW $cm^{-2}$). The probe was inserted into the precursor for 15 min, with scans performed every 3 s and a resolution set at 4 $cm^{-1}$. EPR characterization was performed using a Bruker EPR spectrometer at room temperature, with Ru(II) and APS dissolved in water and DMPO added. The CISDM strategy was stored in the refrigerator before testing. CISSM strategy tested after illumination. Scanning electron microscopy (SEM) imaging was performed on an SU-8010 microscope to observe sample morphologies. Optical microscope observations of the hydrogels were made using a Nikon Eclipse Ni microscope.

Mechanical testing of PEPMN samples (8 mm × 40 mm × 2 mm) was carried out on an MTS Insight 50 tensile clamp at a speed of 50 mm $min^{-1}$ at room temperature. The compression tests were carried out at a speed of 10 mm $min^{-1}$. The radius of the utilized cylindrical samples was 15 mm with a height of 10 mm. Furthermore, the tearing test was used to obtain fracture energy. Hydrogels with a notch (2 mm) were fixed on the equipment and stretched at a speed of 50 mm $min^{-1}$. A humidifier was used nearby to prevent the dehydration of samples. Fatigue thresholds were assessed through cyclic loading tests to evaluate the resistance of hydrogels to crack propagation under repeated stress. Hydrogels with a notch (2 mm) were fixed on the equipment. Cyclic loading was applied at a rate of 50 mm $min^{-1}$. The cyclic strain was gradually increased until crack propagation was observed, ultimately leading to sample fracture. During the test, a humidifier was used to maintain a stable humidity environment and prevent sample dehydration. Stress relaxation and creep tests were conducted to evaluate the time-dependent mechanical behavior of the hydrogels. In the normalized stress relaxation test, the hydrogel sample was subjected to a constant strain of 100%, and the resulting force was monitored as a function of time. This test provides insights into the material's ability to dissipate stress under sustained deformation. For the creep test, a constant force of 0.5 N was applied to the hydrogel, and the resulting strain was measured over time. This test characterizes the material's deformation response under a constant load, reflecting its viscoelastic properties and long-term stability. PEPMN precursor solutions were applied between two pieces of surfaces measuring 25 mm × 25 mm × 0.1 mm, which were affixed to glass slides measuring 2.5 cm × 7.5 cm. The samples were then exposed to visible light (452 nm, 15 mW $cm^{-2}$) for approximately 2 min. The adhesive strength was measured by tensile loading the samples at a rate of 50 mm $min^{-1}$ until detachment occurred. The ultimate adhesive strength at the detachment point was recorded. This process was repeated for controlled trials.

Rheology testing was performed on Anton Paar MCR302 at room temperature with a strain of 1% at 10 Hz. 1 mL of solution was first injected onto the plate (diameter of 25 mm) with a gap of 1,000 μm. Then, the rotor slowly went down and attached to the solution surface. After that, visible light was applied through the transparent quartz plate (15 mW $cm^{-2}$), and the storage and loss modulus were recorded immediately. The gelation process of the hydrogel precursor under blue light was evaluated using a rotational rheometer equipped with optical modules and a 25-mm diameter steel parallel-plate geometry. The testing was performed at room temperature with a strain of 1% at 10 Hz, following 1 min of equilibration (time to gel point defined as the crossover between storage, G′, and loss modulus, G″). The storage modulus G′ and loss modulus G″ were measured as a function of angular frequency ω using a strain-controlled rheometer AR-G2 (TA) with a plate fixture with a diameter of 25 mm. Frequency sweep was performed from 0.1 to 100 rad $s^{-1}$ at a fixed strain amplitude of γ = 0.1% for PEPMNs at 15 °C. Time–temperature superposition (TTS) was applied to construct the master curve for PEPMNs at the reference temperature Tref = 15 °C after a frequency sweep was performed at 15, 20, 25, 30, 35, 40, 45, and 50 °C. Silicone oil was laid on the edge of the plates to prevent water evaporation.

Characterization of Single-Molecular Force Spectroscopy (SMFS). Polymers (i.e., PAAm, ALG, and Gel) were dissolved in DI water at room temperature to prepare a solution with a concentration of 1 mg $L^{-1}$ (pH ~8.6). About 100 μL of the polymer solution was dropped onto a slide surface for 30 min, followed by thorough rinsing with DI water. The sample was then used immediately after being dried with airflow. The force measurements in different liquid environments were conducted on the atomic force microscopy (AFM) (Nanowizard II, JPK Instruments, Germany). A drop of environmental solvents (water or nonane, *ca*. 100 μL) was then injected between the AFM cantilever and the sample. For SMFS experiments conducted in aqueous environments, freshly added DI water was used. Thus, the polymer concentration in force measurements would be much lower, and the pH would be close to neutral. Therefore, the SMFS experiment primarily examines the effects of the local environment on the single-chain behavior of polymer, rather than the bulk solution itself. The spring constants of the V-shaped $Si_3N_4$ AFM (Bruker Corp.) cantilever were estimated by the thermo-excitation method, with values generally falling between 30 and 50 pN $nm^{-1}$. In this range, the influence of the gravity of the tip on the bending of the cantilever can be ignored. The experiments were carried out in a liquid environment between the AFM tip and substrate. The AFM tip was stretched at a speed of 2.0 μm $s^{-1}$ unless mentioned otherwise. To ensure the reproducibility of the single-chain mechanics under the specified conditions, the SMFS experiments were repeated on various batches of samples under identical conditions. The F-E curves obtained in this study were analyzed by Igor ProV6.05 with custom procedures.

The sensitivity of PEPMNs was measured using a two-probe testing assembly with a digital multimeter (Keithley 6517B). Three samples were tested for each composition.

Unless otherwise specified in this experiment, toughness is the integral area of the stress-strain curve, and fracture energy is the product of toughness and the original length of the sample.

Further details on the methods are available in the Supplementary Information.

## Data availability

The data that support the findings of this study are available from the corresponding author on request.

## References

1. Michieletto, D. et al. Topological digestion drives time-varying rheology of entangled DNA fluids. *Nat. Commun.* **13**, 4389 (2022).
2. Smrek, J. et al. Topological tuning of DNA mobility in entangled solutions of supercoiled plasmids. *Sci. Adv.* **7**, eabf9260 (2021).
3. Doyle, L. A. et al. De Novo design of knotted tandem repeat proteins. *Nat. Commun.* **14**, 6746 (2023).
4. Allard, C. Mimicking stiff tissues through chain entanglements. *Nat. Rev. Mater.* **8**, 494–494 (2023).
5. Zhang, Y. et al. Peptide-enhanced tough, resilient and adhesive eutectogels for highly reliable strain/pressure sensing under extreme conditions. *Nat. Commun.* **13**, 6671 (2022).

6. Campise, F. et al. Contribution of entanglements to polymer network elasticity. *Macromolecules* **50**, 2964–2972 (2017).
7. Koner, K. et al. Viscoelastic covalent organic nanotube fabric via macroscopic entanglement. *J. Am. Chem. Soc.* **144**, 16052–16059 (2022).
8. Ma, J. et al. Designing ultratough single-network hydrogels with centimeter-scale fractocohesive lengths via inelastic crack blunting. *Adv. Mater.* **36**, 2311795 (2024).
9. Steck, J. et al. Multiscale stress deconcentration amplifies fatigue resistance of rubber. *Nature* **624**, 303–308 (2023).
10. Bukowski, C. et al. Load-bearing entanglements in polymer glasses. *Sci. Adv.* **7**, eabg9763 (2021).
11. Shi, W. et al. Dynamic-bond-mediated chain reptation enhances energy dissipation of elastomers. *Angew. Chem. Int. Ed.* **63**, e202401845 (2024).
12. Han, Z., Lu, Y. & Qu, S. Design of fatigue-resistant hydrogels. *Adv. Funct. Mater.* **34**, 2313498 (2024).
13. Kuang, X. et al. Functional tough hydrogels: design, processing, and biomedical applications. *Acc. Mater. Res.* **4**, 101–114 (2023).
14. Fu, L. et al. Cartilage-like protein hydrogels engineered via entanglement. *Nature* **618**, 740–747 (2023).
15. Yu, Z. & Wu, P. Underwater communication and optical camouflage ionogels. *Adv. Mater.* **33**, 2008479 (2021).
16. Wang, Z. et al. Hydrogen bonds-pinned entanglement blunting the interfacial crack of hydrogel–elastomer hybrids. *Adv. Mater.* **36**, 2313177 (2024).
17. Zheng, Z. et al. Self-growing hydrogel bioadhesives for chronic wound management. *Adv. Mater.* **36**, 2408538 (2024).
18. Fan, C. et al. 3D printing of lubricative stiff supramolecular polymer hydrogels for meniscus replacement. *Biomater. Sci.* **9**, 5116–5126 (2021).
19. Fang, Z. et al. 3D printable elastomers with exceptional strength and toughness. *Nature* **631**, 783–788 (2024).
20. Chen, G. et al. Printable thermochromic hydrogel-based smart window for all-weather building temperature regulation in diverse climates. *Adv. Mater.* **35**, 2211716 (2023).
21. Sun, L. et al. Cooperative chemical coupling and physical lubrication effects construct highly dynamic ionic covalent adaptable network for high-performance wearable electronics. *CCS Chem.* **5**, 1096–1107 (2023).
22. Ni, C. et al. Shape memory polymer with programmable recovery onset. *Nature* **622**, 748–753 (2023).
23. Guo, B. et al. Haemostatic materials for wound healing applications. *Nat. Rev. Chem.* **5**, 773–791 (2021).
24. Wan, X. et al. Bioinspired structural adhesives: a decades-old science but emerging materials. *Matter* **7**, 1710–1723 (2024).
25. Xie, Q. et al. In situ triggered self-contraction bioactive microgel assembly accelerates diabetic skin wound healing by activating mechanotransduction and biochemical pathway. *Adv. Mater.* **36**, 2406434 (2024).
26. Zhou, X. et al. Reversibly growing crosslinked polymers with programmable sizes and properties. *Nat. Commun.* **14**, 3302 (2023).
27. Hou, L. X. et al. Intrinsic anti-freezing and unique phosphorescence of glassy hydrogels with ultrahigh stiffness and toughness at low temperatures. *Adv. Mater.* **35**, 2300244 (2023).
28. Zheng, Y. et al. Molecular design of stretchable polymer semiconductors: current progress and future directions. *J. Am. Chem. Soc.* **144**, 4699–4715 (2022).
29. Jiao, D. et al. Programmable morphing hydrogels for soft actuators and robots: from structure designs to active functions. *Acc. Chem. Res.* **55**, 1533–1545 (2022).
30. Zhu, Q. L. et al. Animating hydrogel knotbots with topology-invoked self-regulation. *Nat. Commun.* **15**, 300 (2024).
31. Li, T. et al. Healable ionic conductors with extremely low-hysteresis and high mechanical strength enabled by hydrophobic domain-locked reversible interactions. *Adv. Mater.* **35**, 2307990 (2023).
32. Li, X. & Gong, J. P. Design principles for strong and tough hydrogels. *Nat. Rev. Mater.* **9**, 380–398 (2024).
33. Zhong, D. et al. A strategy for tough and fatigue-resistant hydrogels via loose cross-linking and dense dehydration-induced entanglements. *Nat. Commun.* **15**, 5896 (2024).
34. Xu, S. et al. Concurrent stiffening and softening in hydrogels under dehydration. *Sci. Adv.* **9**, eade3240 (2023).
35. Kim, J. et al. Fracture, fatigue, and friction of polymers in which entanglements greatly outnumber cross-links. *Science* **374**, 212–216 (2021).
36. Xu, Z. et al. A self-thickening and self-strengthening strategy for 3D printing high-strength and antiswelling supramolecular polymer hydrogels as Meniscus substitutes. *Adv. Funct. Mater.* **31**, 2100462 (2021).
37. Cho, Y. E. et al. Solvent engineering of thermo-responsive hydrogels facilitates strong and large contractile actuations. *Adv. Mater.* **36**, 2406103 (2024).
38. Choi, W. & Kohane, D. S. Hybrid nanoparticle–hydrogel systems for drug delivery depots and other biomedical applications. *ACS Nano* **18**, 22780–22792 (2024).
39. Huang, J., Yu, Z. & Wu, P. 3D printing of ionogels with complementary functionalities enabled by self-regulating ink. *Adv. Sci.* **10**, 2302891 (2023).
40. Liu, C. et al. Tough hydrogels with rapid self-reinforcement. *Science* **372**, 1078–1081 (2021).
41. Meng, X. et al. Hysteresis-free nanoparticle-reinforced hydrogels. *Adv. Mater.* **34**, 2108243 (2022).
42. Li, W. et al. Nanoconfined polymerization limits crack propagation in hysteresis-free gels. *Nat. Mater.* **23**, 131–138 (2024).
43. Hart, L. F. et al. Material properties and applications of mechanically interlocked polymers. *Nat. Rev. Mater.* **6**, 508–530 (2021).
44. Liu, P. et al. Peptide-crosslinked, highly entangled hydrogels with excellent mechanical properties but ultra-low solid content. *Adv. Mater.* **35**, 2210021 (2023).
45. Zhu, R. et al. Tough double network hydrogels with rapid self-reinforcement and low hysteresis based on highly entangled networks. *Nat. Commun.* **15**, 1344 (2024).
46. Dhand, A. P. et al. Additive manufacturing of highly entangled polymer networks. *Science* **385**, 566–572 (2024).
47. Chen, L. et al. A hyperelastic hydrogel with an ultralarge reversible biaxial strain. *Science* **383**, 1455–1461 (2024).
48. Gong, J. P. et al. Double-network hydrogels with extremely high mechanical strength. *Adv. Mater.* **15**, 1155–1158 (2003).
49. Guo, X. et al. Fracture-resistant stretchable materials: an overview from methodology to applications. *Adv. Mater.* **37**, 2312816 (2025).
50. Huang, B., Nian, S. & Cai, L.-H. A universal strategy for decoupling stiffness and extensibility of polymer networks. *Sci. Adv.* **10**, eadq3080 (2024).
51. Guo, X. et al. Strong and tough fibrous hydrogels reinforced by multiscale hierarchical structures with multimechanisms. *Sci. Adv.* **9**, eadf7075 (2023).
52. Truong, V. X. et al. Wavelength-orthogonal stiffening of hydrogel networks with visible light. *Angew. Chem. Int. Ed.* **61**, e202113076 (2022).
53. Binyamin, I. et al. 3D printing thermally stable high-performance polymers based on a dual curing mechanism. *Adv. Funct. Mater.* **33**, 2214368 (2023).
54. Bernaerts, K. V. & Du Prez, F. E. Dual/heterofunctional initiators for the combination of mechanistically distinct polymerization techniques. *Prog. Polym. Sci.* **31**, 671–722 (2006).

55. Irvine, G. et al. Highly entangled hydrogels by photoiniferter-mediated polymerization. *Angew. Chem. Int. Ed.*, e202421970 (2025).
56. Qiao, H. et al. Entropy-driven design of highly impact-stiffening supramolecular polymer networks with salt-bridge hydrogen bonds. *J. Am. Chem. Soc.* **146**, 7533–7542 (2024).
57. Wang, C. et al. Visible-light-assisted multimechanism design for one-step engineering tough hydrogels in seconds. *Nat. Commun.* **11**, 4694 (2020).
58. Wei, H. et al. Orthogonal photochemistry-assisted printing of 3D tough and stretchable conductive hydrogels. *Nat. Commun.* **12**, 2082 (2021).
59. Liu, J. et al. Designing tough, printable, and adaptable eutectogels with multinetworks via synergy of rapid orthogonal photopolymerizations and solvent effect in seconds. *CCS Chem.* **6**, 390–402 (2024).
60. Liu, G. et al. Influence of chain entanglement on rheological and mechanical behaviors of polymerized ionic liquids. *Macromolecules* **56**, 2719–2728 (2023).
61. Virág, Á. D. et al. Combining oscillatory shear rheometry and dynamic mechanical analysis to obtain wide-frequency master curves. *Polymer* **295**, 126742 (2024).
62. Wang, Z. et al. Physical-entanglements-supported polymeric form stable phase change materials with ultrahigh melting enthalpy. *Adv. Mater.* **36**, 2108243 (2024).
63. Sun, J.-Y. et al. Highly stretchable and tough hydrogels. *Nature* **489**, 133–136 (2012).
64. Wu, J. et al. Adhesive anti-fibrotic interfaces on diverse organs. *Nature* **630**, 360–367 (2024).
65. Cintron-Cruz, J. A. et al. Rapid ultratough topological tissue adhesives. *Adv. Mater.* **34**, 2205567 (2022).
66. Xu, Z. et al. Rapidly damping hydrogels engineered through molecular friction. *Nat. Commun.* **15**, 4895 (2024).

## Acknowledgements

The authors acknowledge the National Natural Science Foundation of China (Grant no. 22175141) and the Nature Science Foundation of Shaanxi Province (Grant nos. 2023-JC-JQ-14, 2023JC-XJ-21, and 2022JQ-146) for the financial support of this work. The authors thank Prof. Shuxun Cui and Prof. Yu Bao (Northeastern University, China) for single molecular force spectroscopy characterization.

## Author contributions

A.W. and Q.W. contributed equally to this work. Y.Y. conceived the idea and designed the research. A.W. and Q.W. prepared materials and performed optical and mechanical characterizations. T.W. performed the time–temperature superposition testing experiment. J.L. and Y.Y. analyzed and interpreted the results. Y.H., H.L., Z.Z., and Y.Y. drafted the paper and all authors contributed to the writing of the paper.

## Competing interests

The authors declare no competing interests.

## Additional information

**Supplementary information** The online version contains supplementary material available at https://doi.org/10.1038/s41467-025-59669-3.

**Correspondence** and requests for materials should be addressed to You Yu.

**Peer review information** *Nature Communications* thanks Yongjun Zhang and the other, anonymous, reviewers for their contribution to the peer review of this work. A peer review file is available